Journal of Wind Engineering & Industrial Aerodynamics 257 (2025) 105991

Contents lists available at ScienceDirect

Journal of Wind Engineering & Industrial Aerodynamics

journal homepage: www.elsevier.com/locate/jweia

Numerical study of turbulent flows over complex terrain using an unsteady Reynolds-averaged Navier-Stokes model with a new method for turbulent inflow generation

Xiangyan Chen, Takeshi Ishihara *

Department of Civil Engineering, School of Engineering, The University of Tokyo, Tokyo, 113-8656, Japan

ARTICLE INFO

Keywords:
Complex terrain
URANS
Turbulent inflow
Averaging time
Mean velocity
Standard deviation

ABSTRACT

In this study, an unsteady Reynolds-Averaged Navier-Stokes (URANS) model with a prespecified averaging time and a new method for turbulent inflow generation is proposed to predict turbulent flows over complex terrain. Firstly, the effect of grid resolution on turbulent flows over complex terrain is investigated by the Reynolds-Averaged Navier-Stokes (RANS) and the URANS models. URANS improves the accuracy of the predicted mean velocity and standard deviation by using finer grids, but the improvement by RANS is limited. Furthermore, the turbulent flows over hills with different slopes predicted by URANS are examined with respect to various averaging times. An optimal averaging time based on the slope of the hills is recommended considering the prediction accuracy and computational efficiency of URANS. Finally, turbulent flows over complex terrain in coastal areas are investigated by URANS and validated by wind tunnel tests. The predicted mean and standard deviation of streamwise velocity over complex terrain by URANS are in good agreement with the experimental data, while those by RANS are overestimated or underestimated.

1. Introduction

The development of wind turbines has been characterized by an increase in capacity. Regarding micro-siting of a wind farm, it is essential to assess the mean wind speed and turbulence intensity. The mean wind speed is important for assessing the overall wind energy potential of a site since wind power is proportional to the cube of mean wind speed. On the other hand, turbulence intensity can have a significant impact on the performance of wind turbines, including wind turbine loading, structural integrity, and fatigue life. Accurate prediction of the turbulent flow field is therefore crucial for the proper design, control strategies, and optimization of wind farm layouts (Watanabe and Uchida, 2015; Ishihara and Qi, 2019; Qian and Ishihara, 2019).

Nowadays, Computational Fluid Dynamics (CFD) has been widely employed for micro-siting of a wind farm because it can provide detailed information on mean wind speeds, turbulence, and wake effects in wind farms. Typically, numerical simulations with multiple wind directions need to be conducted to comprehensively evaluate the performance of wind farms (Yamaguchi et al., 2003; Liu et al., 2016; Ishihara et al., 2020), resulting in high demands on computational resources. Blocken et al. (2015) stated that steady Reynolds-Averaged Navier-Stokes (RANS) has remained the predominant turbulence model to date since the computational cost of Large Eddy Simulation (LES) is one or two orders of magnitude larger than RANS. On the other hand, RANS can significantly improve computational efficiency compared to LES, but its prediction accuracy is not guaranteed. Unsteady Reynolds-Averaged Navier-Stokes (URANS) is a bridge between RANS and LES that considers both prediction accuracy and computational efficiency. However, as pointed out by Ishihara and Qi (2019), when a steady inflow is employed, URANS performs similarly to RANS. Therefore, an unsteady inflow is needed to realize the potential of URANS to simulate turbulent flow over complex terrain.

Except for the turbulence model, grid size and time step also affect the accuracy of numerical simulations over complex terrain. Grid sizes vary from 6 m to 22 m over real terrains as shown in Table 1, where the length scale is used to express grid sizes at full scale. Overall, the grid resolution of LES is significantly higher than that of RANS. The main reason is that the accuracy and reliability of LES, Delayed Detached-Eddy Simulations (DDES) (Ishihara and Qi, 2019) and Detached-Eddy Simulations (DES) (Zhou et al., 2022) are affected by the grid size, since turbulent structures larger than the grid size are explicitly resolved, whereas turbulent structures smaller than the grid size are

* Corresponding author.
E-mail addresses: x.chen@bridge.t.u-tokyo.ac.jp (X. Chen), ishihara@bridge.t.u-tokyo.ac.jp (T. Ishihara).

https://doi.org/10.1016/j.jweia.2024.105991
Received 9 September 2024; Received in revised form 16 November 2024; Accepted 2 December 2024

Table 1
Description of turbulence models, terrain types, scales, grid sizes and time steps used in previous numerical simulations over ridges, hills and complex terrain.

No.	References	Turbulence model	Terrain Type	Scale	Grid size	Time step
1	Iizuka and Kondo, 2004	LES	2D ridge	1:1000	2 m	1 s
2	Bechmann and Sorensen, 2011	RANS/LES	Real terrain	1:1	31 m	0.5 s
3	Liu et al. (2016)	LES	Real terrain	1:2000	6 m	0.2 s
4	Ren et al. (2018)	LES	Real terrain	1:1	6.25 m	–
5	Ishihara and Qi (2019)	DDES	2D ridge/3D hill	1:1000	2 m	0.1 s
6	Qian and Ishihara (2019)	DDES	Real terrain	1:1	8 m	0.2 s
7	Yang et al. (2021)	LES	3D hill	1:1000	2 m	0.1 s
8	Hu et al. (2021)	LES	Real terrain	1:1000	–	1 s
9	Zhou et al. (2022)	DES	3D hill	1:1000	3 m	0.1 s
10	Li et al. (2024)	LES	Real terrain	1:2200	22 m	2.2 s
11	Yamaguchi et al. (2024)	LES	Real terrain	1:1	8 m	0.1 s
12	Ishihara and Hibi (2002)	RANS	3D hill	1:1000	6 m	–
13	Yamaguchi et al. (2003)	RANS	Real terrain	1:2000	25 m	–
14	Blocken et al. (2015)	RANS	Real terrain	1:1	25 m	–
15	Huang and Zhang (2019)	RANS	Real terrain	1:4000	20 m	–
16	Chen et al. (2020)	RANS	Real terrain	1:1500	6.5 m	–
17	Cheynet et al. (2020)	RANS	Real terrain	1:1	10 m	–
18	Wang et al. (2024)	RANS	Real terrain	1:1	12.5 m	–
19	Cheng et al. (2024)	RANS	Real terrain	1:1	12.5 m	–
20	Bao et al. (2024)	RANS	Real terrain	1:1	40 m	–

modelled (Bechmann and Sorensen, 2011; Ishihara and Qi, 2019; Bhuiyan and Alam, 2020; Yang et al., 2021a,b; Zhou et al., 2022; Li et al., 2024). As a result, finer grid resolutions can provide a more detailed representation of the turbulent flows, but at a higher computational cost (Chapman, 1979; Spalart et al., 1997; Beare et al., 2004). Conversely, the grid resolution for RANS is usually coarser than that of LES and DDES in directions where the mean flow changes slowly (Li et al., 2022). This is because the turbulence in RANS is modelled using time-averaged equations, and the turbulent structures are not explicitly resolved (Vijiapurapu and Cui, 2010; Bechmann and Sorensen, 2011; Chipongo et al., 2020).

Furthermore, LES requires a small-time step to capture the turbulent structures as shown in Table 1, where the velocity scale is assumed as 1 and the time step is expressed at full scale. URANS aims to capture the mean flow and statistical turbulence characteristics, and therefore can use a larger time step than LES. However, previous studies using URANS have not been investigated in detail. Since coherent structures, such as vortex shedding, exist behind steep terrain. An appropriate averaging time in URANS simulation is crucial to meet the requirements of both prediction accuracy and computational efficiency, and the relationship between the optimal averaging time and the terrain slope requires further investigation.

This study aims to (1) propose an unsteady Reynolds-Averaged Navier-Stokes (URANS) model with a prespecified averaging time and a turbulent inflow generation method, (2) provide optimal grid sizes and averaging times to accurately and efficiently predict turbulent flows over complex terrain, (3) clarify the turbulent flow patterns over complex terrain, such as, the flow separation, recirculation and wake in complex terrain using the proposed URANS model with the optimized parameters. Section 2 describes numerical models, including governing equations and numerical scheme, the prespecified averaging time and unsteady inflow used in URANS, and indicators to evaluate the performance of turbulence model. Section 3 first describes complex terrain and three-dimensional hills investigated, then presents the unsteady inflow used in this study and investigates the grid independence of URANS and the optimal averaging time for different terrain slopes considering the prediction accuracy and computational efficiency. Finally, the mean and standard deviation of streamwise velocity over complex terrain predicted by URANS is validated by wind tunnel tests and compared with those by RANS to reveal the performance of turbulence models in Section 4. The conclusions are summarized in Section 5.

2. Numerical methods

An unsteady Reynolds-Averaged Navier-Stokes model (here after referring to URANS) and a new method for turbulent inflow generation are proposed in Sections 2.1 and 2.2. The indicators for evaluating performance of turbulence models are introduced in Section 2.3.

2.1. Governing equations and turbulence model

The governing equations for continuity and momentum in incompressible flow are expressed as,

$$\frac{\partial(\rho\widetilde{u}_i)}{\partial x_i}=0 \tag{1}$$

$$\rho\frac{\partial\widetilde{u}_i}{\partial t}+\rho\frac{\partial(\widetilde{u}_j\widetilde{u}_i)}{\partial x_j}=-\frac{\partial\widetilde{p}}{\partial x_i}+\frac{\partial}{\partial x_j}\left[\mu\left(\frac{\partial\widetilde{u}_i}{\partial x_j}+\frac{\partial\widetilde{u}_j}{\partial x_i}\right)\right]-\rho\frac{\partial(\widetilde{u_iu_j})}{\partial x_j} \tag{2}$$

where $\widetilde{u}_i(t)$ is the resolved velocity in the i direction ($i=1, 2, 3$). $\widetilde{p}$ is the resolved pressure. ρ is the air density and μ is the molecular viscosity. The stress $\widetilde{u_iu_j}$ in Eq. (2) is usually modelled by eddy-viscosity hypothesis and is expressed as,

$$\widetilde{u_iu_j}=2\mu_t\widetilde{S}_{ij}+\frac{\delta_{ij}}{3}\widetilde{u_ku_k} \tag{3}$$

$$\widetilde{S}_{ij}=\frac{1}{2}\left(\frac{\partial\widetilde{u}_i}{\partial x_j}+\frac{\partial\widetilde{u}_j}{\partial x_i}\right) \tag{4}$$

where δ_{ij} is the Kronecker delta function. μ_t is the turbulence viscosity and can be written as,

$$\mu_t=C_\mu\rho\frac{k_S^2}{\varepsilon_S} \tag{5}$$

where k_S and ε_S are the modelled turbulent kinetic energy and turbulent dissipation rate, which are computed from the transport equations as follows:

$$\frac{\partial\rho k_S}{\partial t}+\frac{\partial\rho\widetilde{u}_jk_S}{\partial x_j}=\frac{\partial}{\partial x_j}\left[\left(\mu+\frac{\mu_t}{\sigma_k}\right)\frac{\partial k_S}{\partial x_j}\right]-\rho\widetilde{u_iu_j}\frac{\partial\widetilde{u}_j}{\partial x_i}-\rho\varepsilon_S \tag{6}$$

$$\frac{\partial \rho \varepsilon_S}{\partial t}+\frac{\partial \rho \widetilde{u}_j \varepsilon_S}{\partial x_j}=\frac{\partial}{\partial x_j}\left[\left(\mu+\frac{\mu_t}{\sigma_\varepsilon}\right)\frac{\partial \varepsilon_S}{\partial x_j}\right]-C_{\varepsilon 1}\rho\widetilde{u_i u_j}\frac{\partial \widetilde{u}_j}{\partial x_i}\frac{\varepsilon_S}{k_S}-C_{\varepsilon 2}\frac{\rho\varepsilon_S^2}{k_S}-\frac{C_\mu \rho \eta^3\left(1-\frac{\eta}{\eta_0}\right)}{1+\beta\eta^3}\frac{\varepsilon_S^2}{k_S}+S_\varepsilon \tag{7}$$

where σ_k and σ_ε are constant for modelled turbulence kinetic energy k_S and modelled turbulence dissipation rate ε_S, respectively. The default constants in transport equations are $C_{\varepsilon 1}=1.42$, $C_{\varepsilon 2}=1.68$, $C_{\varepsilon 3}=1.5$, $C_\mu=0.0845$, $\sigma_k=\sigma_\varepsilon=1.393$, $\eta_0=4.38$, $\beta=0.012$. $\eta\equiv|\widetilde{S}|k_S/\varepsilon_S$ and $|\widetilde{S}|=\sqrt{\widetilde{S}_{ij}\widetilde{S}_{ij}}$. The fourth term on the right-hand side of Eq. (7) is from the RNG k-ε model (Yakhot and Orszag, 1986), which aims to quantify the effects of rapid strain and streamline curvature. The model parameters in the RNG k-ε model differ from those used in the standard k-ε model and the reason for this difference was explained by Yakhot and Smith (1992) because it contains the fourth term Eq. (7) that is small in weakly strained turbulence and large in rapidly distorted flows.

The fifth term S_ε on the right-hand side of Eq. (7) is from STRUCT-ε model (Xu, 2020), which is the product of a constant $C_{\varepsilon 3}$, modelled turbulent kinetic energy k_S and the second invariant of the resolved velocity gradient tension, $\widetilde{II}$ used to describe regions lack applicability of the scale-separation assumption as follows:

$$S_\varepsilon=C_{\varepsilon 3}k_S\widetilde{II}=-\frac{C_{\varepsilon 3}k_S}{2}\frac{\partial \widetilde{u}_i}{\partial x_j}\frac{\partial \widetilde{u}_j}{\partial x_i} \tag{8}$$

The constant $C_{\varepsilon 3}$ of 1.5 is determined by a sensitivity study by Xu (2020) and is used to predict the flow fields around the freight train and T-junction by García et al. (2020) and Feng et al. (2021). Although the STRUCT-ε model improves the overestimation of turbulence viscosity in the wake region, it has only been used for the flow fields with smooth inflow. By combining the turbulent inflow generation method presented in Section 2.2 with Eqs. (6) and (7), both prediction accuracy and computational efficiency can be achieved for the flow fields with turbulent inflow.

The numerical simulations are performed using Fluent (2021). The spatial discretization method employed is second order upwind. Regarding the time discretization methods, a second order implicit scheme is used. Additionally, the pressure-velocity coupling follows the Semi-Implicit Pressure Linked Equations (SIMPLE) approach. The outlet boundary condition is set as a pressure outlet. Symmetry conditions are applied to the side and top boundaries. The bottom surface, including the complex terrain, is defined as a non-slip wall with a surface roughness.

2.2. Generation of unsteady inflow for URANS

As pointed out by Ishihara and Qi (2019), if steady inflow is employed, the mean and turbulent fields predicted by URANS are same as those by RANS. Therefore, it is essential to develop a method to generate unsteady inflows for URANS. Fig. 1 shows the flowchart of three steps to generate unsteady inflow.

Firstly, numerical simulations over flat terrain are carried out by LES to export the instantaneous velocity component $u_i(t)=[u_{i,1},u_{i,2},\ldots,u_{i,j},\ldots,u_{i,n}]$, where i denotes the velocity component in the i direction, j is the j th data point and n is the total amount of data points, as shown in Fig. 1 (a).

Secondly, a low-pass filter as shown in Fig. 1 (b) is utilized to filter out the high-frequency fluctuating velocity component based on the prespecified averaging time and separate the turbulent flow field into the resolved and modelled parts. The low-pass filter used in this paper is the moving average with a window d, which is related to the smoothness of the filtered velocity and determined as follows:

$$d=2t_{ave}/dt \tag{9}$$

where dt is the time interval of the original dataset $u_i(t)$ and t_{ave} is the averaging time, which is used as a time step in the proposed URANS model. The resolved velocity $\widetilde{u}_{i,j}$, modelled turbulence kinetic energy $k_{s,j}$, and dissipation rate $\varepsilon_{s,j}$ at the jth data point are calculated as follows:

$$\widetilde{u}_{i,j}=\frac{1}{d+1}\sum_{j-d/2}^{j+d/2}u_{i,j} \tag{10}$$

$$k_{s,j}=\frac{1}{2}\sum_{i=1}^{3}\left(\frac{1}{d+1}\sum_{j-d/2}^{j+d/2}\left(u_{i,j}-\widetilde{u}_{i,j}\right)^2\right) \tag{11}$$

$$\varepsilon_{s,j}=\frac{C_\mu^{3/4}k_{s,j}^{3/2}}{\kappa z} \tag{12}$$

where $u_{i,j}$ and $\widetilde{u}_{i,j}$ are the instantaneous velocity and mean wind velocity in the i direction at the jth data point. After applying the moving average,

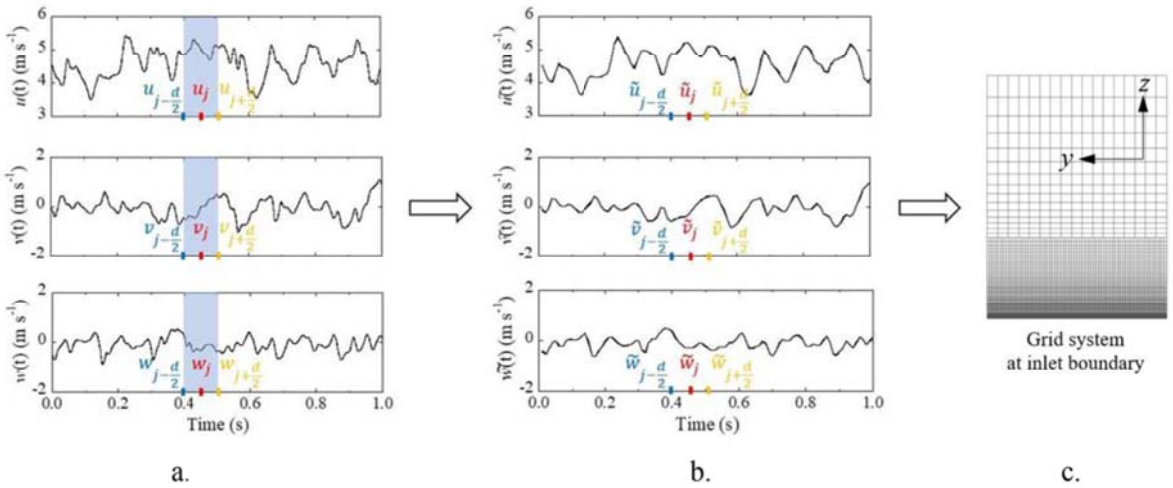

Fig. 1. The flowchart of the proposed unsteady inflow generation method; (a) Instantaneous velocity components; (b) Moving-averaged velocity components; (c) Inlet grid.

the high-frequency fluctuation in the instantaneous velocity is filtered out by Eq. (10). According to Eqs. (11) and (12), the resolved turbulence kinetic energy and dissipation rate are filtered out, while the modelled those are calculated.

Finally, as shown in Fig. 1 (c), the resolved velocity $\widetilde{u}_{i,j}$, modelled turbulence kinetic energy $k_{s,j}$ and dissipation rate $\varepsilon_{s,j}$ after the moving average are imported to the inlet grid. The dataset of resolved velocity, $\left[\widetilde{u}_{i,1},\widetilde{u}_{i,2},\ldots,\widetilde{u}_{i,j},\ldots,\widetilde{u}_{i,m}\right]$, has a total number of data points $m = n\Delta t/\, t_{ave}$. The total time of resolved velocities is equal to the total time of original velocities by LES simulations. The total turbulence kinetic energy K equals to the summation of the modelled turbulence kinetic energy k_s and the resolved turbulence kinetic energy, $\widetilde{k} = \sum\left(\widetilde{u_i u_i}\right)/2$.

Unlike LES, which separates resolved and modelled turbulence by grid resolution limitations (Luis, 2012), URANS separates the two components by time scales. This is achieved by defining a specific averaging time t_{ave} in the process of turbulent inflow generation. The averaging time proposed in this study is related to the window width of the low-pass filter. As pointed out by Israel (2023), filtering a fully resolved turbulent field with any low-pass filter characterized by a specified length scale results in a filtered velocity field, where unsteady fluctuations can be introduced into the initial conditions. Therefore, the subgrid cutoff of URANS depends on the specific averaging time.

Furthermore, if only predicted mean wind speed and standard deviations are desired in application usages, the window width d shown in Eq. (9) can be set to a very large value, which makes the filtered unsteady inflow become a steady inflow and the URANS results will be the same as the RANS results as shown in Qian and Ishihara (2019).

2.3. Indicators for evaluating performance of turbulence models

In this study, two indicators are used to evaluate prediction accuracy and computational efficiency of turbulence models. In terms of prediction accuracy, hit rate (Schatzmann et al., 2010; Oettl, 2015; Ishihara and Qi, 2019) is employed in this study and written as,

$$q = \frac{1}{N}\sum_{i=1}^{N} n_i,\ with\ n_i = \begin{cases} 1, \left|\dfrac{y_i - x_i}{x_i}\right| \le D_q\ or\ |y_i - x_i| \le 0.05|max| \\ 0, else \end{cases} \tag{13}$$

where x_i and y_i are the observed and predicted results, respectively and i is the *ith* results. N represents the total number of predicted or observed values. For the mean wind speed, D_q is 0.15. while for the turbulence kinetic energy, D_q is 0.3 (Ishihara and Qi, 2019). $|max|$ refers to the maximum value among the predicted and observed values. A hit rate of $q = 1$ indicates perfect prediction, meaning that all errors in the numerical results are within the threshold specified in Eq. (13). Conversely, if all errors in the numerical results exceed the threshold, then $q = 0$.

The score of prediction accuracy is quantified by the hit rate as shown in Eq. (14).

$$S_a = \begin{cases} 1, q_U \ge 0.85\ and\ q_K \ge 0.80 \\ 0, others \end{cases} \tag{14}$$

where q_U is the hit rate of the mean wind speed and q_K is the hit rate of the total turbulent kinetic energy K.

The performance of computational efficiency is assessed by the ratio of computational time of any turbulence model to that of RANS. Since RANS is widely recognized for its excellent performance, the score of computational efficiency is evaluated by the ratio of computational time of URANS to that of RANS as shown in Eq. (15).

$$S_e = \begin{cases} 1, T/T_{RANS} \in (16, 32] \\ 2, T/T_{RANS} \in (8, 16] \\ 3, T/T_{RANS} \in (4, 8] \\ 4, T/T_{RANS} \in (2, 4] \\ 5, T/T_{RANS} \in (1, 2] \end{cases} \tag{15}$$

where T is the computational time of any turbulence model and T_{RANS} is the computational time of RANS. The cluster computing system used in this study is Intel Xeon CPU E5-2667 v4 with 88 cores and 960 GB memory.

Referring to the criteria proposed by Lenci (2016) for evaluating any turbulence model, the important considerations of prediction accuracy and computational efficiency are selected to evaluate turbulent models. The score that considers both prediction accuracy and computational efficiency is expressed as follows:

$$S = S_a \times S_e \tag{16}$$

As stated by Blocken (2014), the prediction accuracy of numerical simulations is important, thus the sensitivity of S_a in Eq. (14) is set higher than the sensitivity of computational efficiency in Eq. (15). Meanwhile, S_e is scored from 1 to 5 by dividing computational time of turbulence models by that of RANS because the computational time of RANS is minimal. The smaller the ratio of computational time of other turbulence models to that of RANS, the more computationally efficient the turbulence model is, and the higher the score S_e.

The highest score S is 5, indicating that both accuracy and efficiency criteria are satisfied. The lowest score S is 0, indicating that the accuracy criterion is not met. An acceptable score for both accuracy and efficiency in engineering applications is defined as $S \ge 3$ in this study.

3. Independence tests for grid size and averaging time

Section 3.1 describes the complex terrain in coastal areas and three-dimensional hills in detail. The computational domain of complex terrain is described in Section 3.2. Unsteady inflow and the grid independence are investigated in Sections 3.3. The optimal averaging time for different terrain slopes is examined in Sections 3.4.

3.1. Description of complex terrain and three-dimensional hills

In this study, two types of terrain models are used to investigate the performance of the proposed URANS model: One is a simple three-

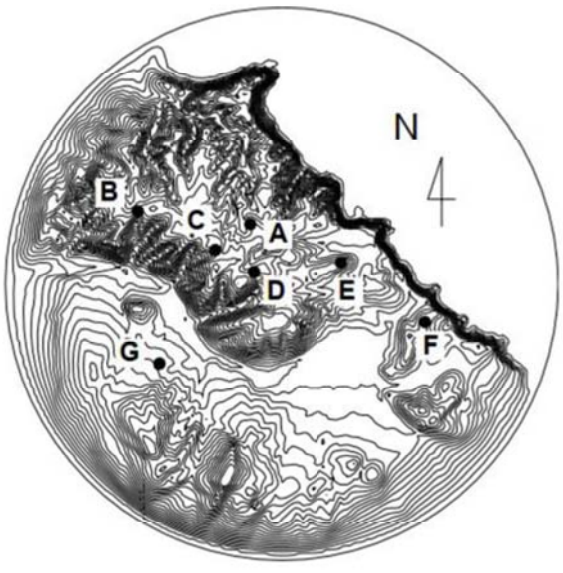

Fig. 2. Elevation contours of complex terrain and measurement points used in this study.

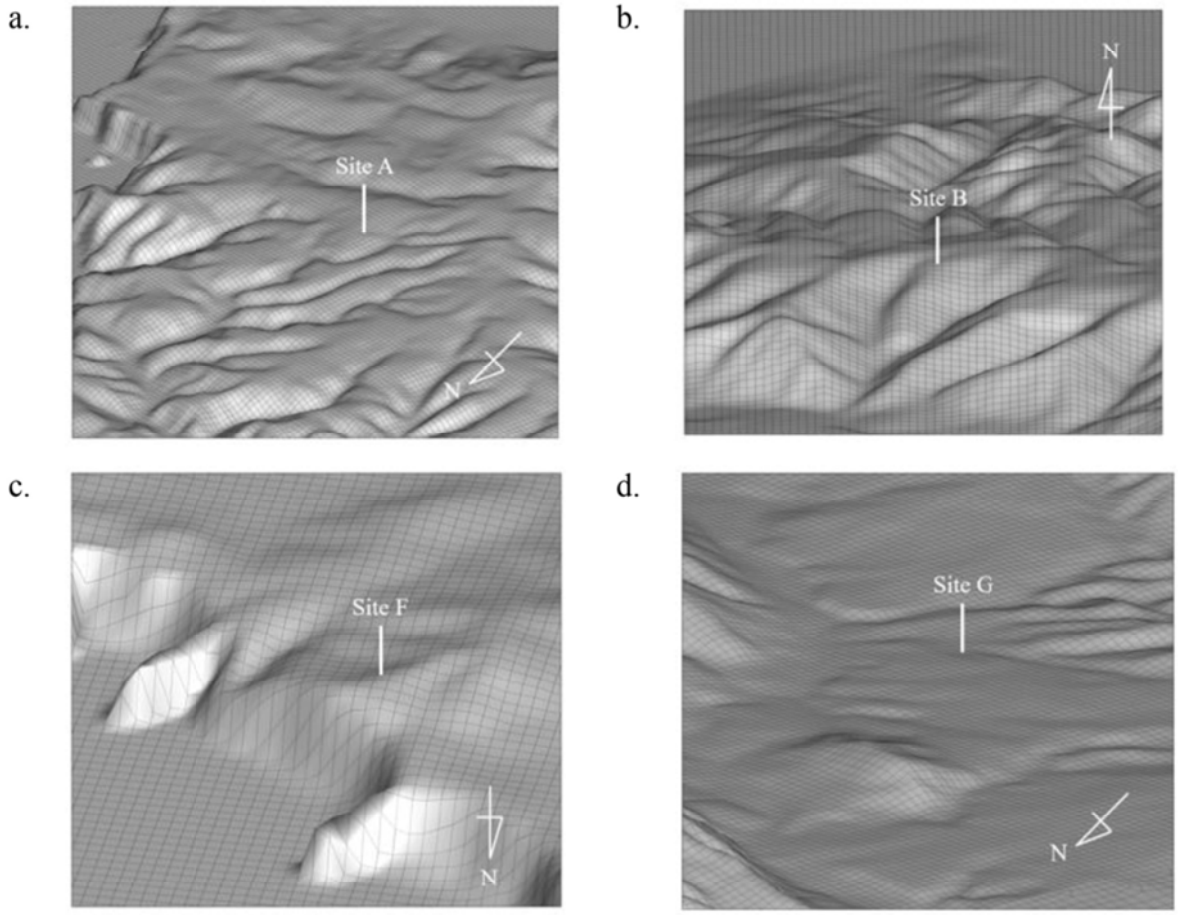

Fig. 3. Bird's eye view of complex terrain around (a) point A, (b) point B, (c) point F and (d) point G.

Table 2
Summary of terrain slope index of measurement points A, B, F and G based on IEC61400-1.

Measurement point	Terrain slope index (°)	Terrain complexity category
A	7.4	L
B	20.9	H
F	36.8	H
G	6.2	L

dimensional hill, the other is a complex terrain.

Elevation contours and measurement points for the complex terrain used in this study are shown in Fig. 2. Points A-G in the figure correspond to the measurement points described in Yamaguchi et al. (2003). Fig. 3 shows Bird's eye view of terrain around four typical measurement points. The surrounding terrains at the measurement points A, B, F and G are quite different. The area around measurement point A is relatively flat and terrain is not complex. Measurement point G is relatively low in elevation and flat but is surrounded by complex terrain. On the other hand, the area around measurement point B is recessed and characterized by complex terrain. To the northeast of measurement point F, a steep cliff runs parallel to the sea. The maximum elevation of the coastal area is 267.4 m. Wind speeds were measured at eight different heights above ground level of 5, 10, 20, 35, 50, 75, 100 and 150 m at full scale as shown in Yamaguchi et al. (2003).

Table 2 summarizes the terrain slope index (TSI) of measurement points A, B, F and G based on the definition in IEC61400-1 (2019). As shown in Fig. 3 and Table 2, the terrain around measurement points A and G is relatively gentle, while the terrain around measurement points B and F is very complex. Therefore, the four measurement points are categorized into two groups based on the gentle and steep terrain.

Since the complexity of coherent structures increases with increasing the terrain slope, the optimal averaging time of URANS needs to be adjusted accordingly. A simple three-dimensional hill as shown in Fig. 4

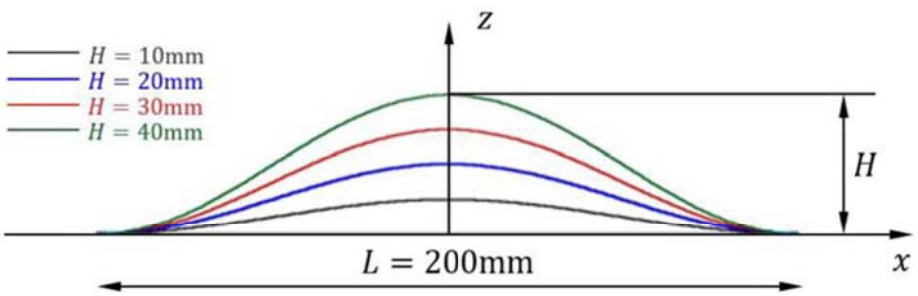

Fig. 4. Configuration of the cross section of the three-dimensional hills with different hill heights.

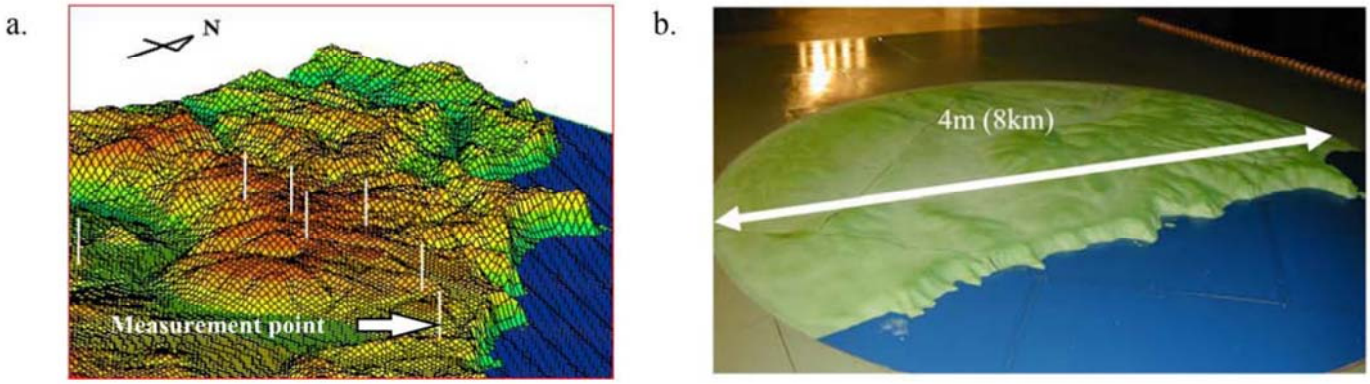

Fig. 5. Elevation of (a) complex terrain and photo of (b) terrain model used in this study.

is employed and expressed as:

$$z_s(x,y)=\begin{cases} H\cos^2\left(\dfrac{\pi\sqrt{x^2+y^2}}{L}\right), \sqrt{x^2+y^2}<\dfrac{L}{2} \\ 0, \sqrt{x^2+y^2}\geq\dfrac{L}{2} \end{cases} \tag{17}$$

where x, y and z are the streamwise, lateral and vertical coordinates, respectively. The center of the hill is at $x=0$, $y=0$. $L=200$ mm is the diameter of the hill. The wind speed over the flat terrain at $z=80$ mm and $x=0$ mm is used as a reference velocity U_{ref} and it is 4.8 m/s as shown in Ishihara et al., (1999) and Ishihara and Qi (2019).

3.2. Computational domain of complex terrain

Fig. 5 shows the configuration of complex terrain along the coast of Hokkaido, Japan and the wind tunnel model used in Yamaguchi et al. (2003). The wind speed outside the boundary layer, U_{ref}, is 6 m/ s. The scale of terrain model is 1:2000 and the diameter at full scale is 8.0 km. The elevation of the terrain model gradually decreases to 0 m at the edge of the terrain model. The height of terrain model $\widehat{z}_s(x,y)$ is calculated as follows:

$$\widehat{z}_s(x,y)=\begin{cases} z_s(x,y), & \sqrt{x^2+y^2}\leq R \\ z_s(x,y)\left[1-\dfrac{\left(\sqrt{x^2+y^2}-R\right)}{L_r}\right]=0, & R\leq\sqrt{x^2+y^2}\leq R+L_r \\ 0, & \sqrt{x^2+y^2}\geq R+L_r \end{cases} \tag{18}$$

where x and y represent the streamwise and lateral coordinates, and the origin of the coordinate system is at the center of the terrain model. $z_s(x,y)$ is the elevation of the original terrain. $R=3.0$ km is the radius of the same extent as the original terrain, $L_r=1.0$ km is the width of the outer ring. The surface roughness length of the terrain at full scale is 0.02 m. The second vertical coordinate, $z'=z-z_s(x,y)$, is also used to indicate the height above the ground surface.

The computational domain for the complex terrain of coastal region is illustrated in Fig. 6 (a). Its extent is 13.5 km × 17.4 km × 2.0 km in the streamwise, lateral and vertical directions, respectively. Fig. 6 (b) shows the grid system. A target zone is a square region with a side of 6.0 km centered at the origin, which is used to investigate the effects of the complex terrain on the turbulent flow fields. An additional zone is connected in front of the target zone to consider the effect of upstream terrain. A buffer zone surrounding the additional zone along and the target region is provided to prevent the effect of side and downstream boundaries. The σ grid system is employed to adjust the vertical coordinates above the terrain and to keep the ratio of vertical grid size constant. The vertical grid size of the first layer is 0.4 m at full scale with

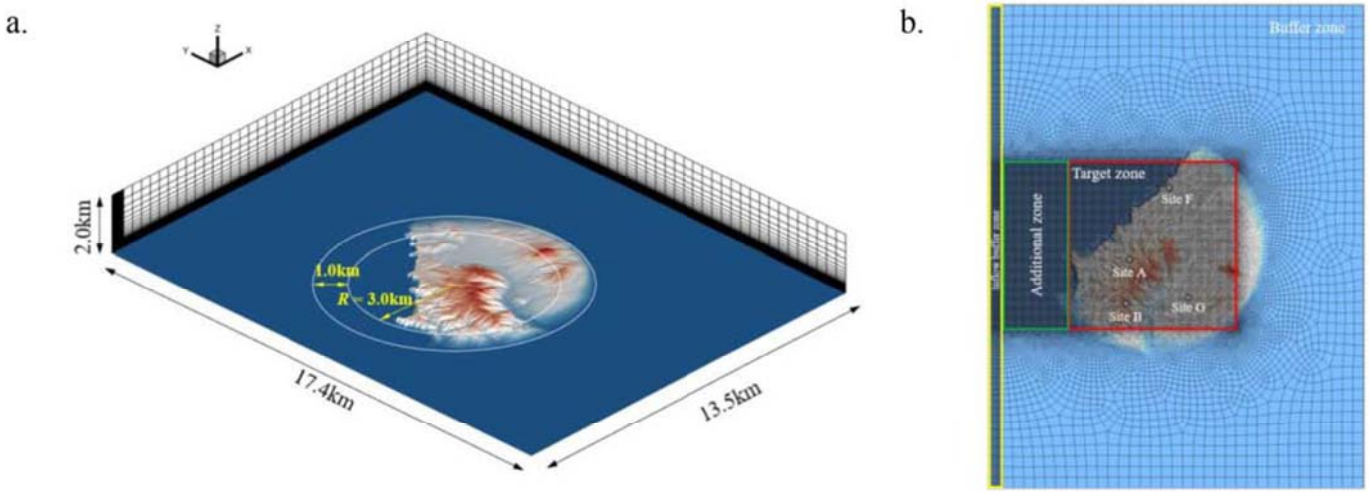

Fig. 6. Configuration of (a) computational domain and (b) top view of grid system.

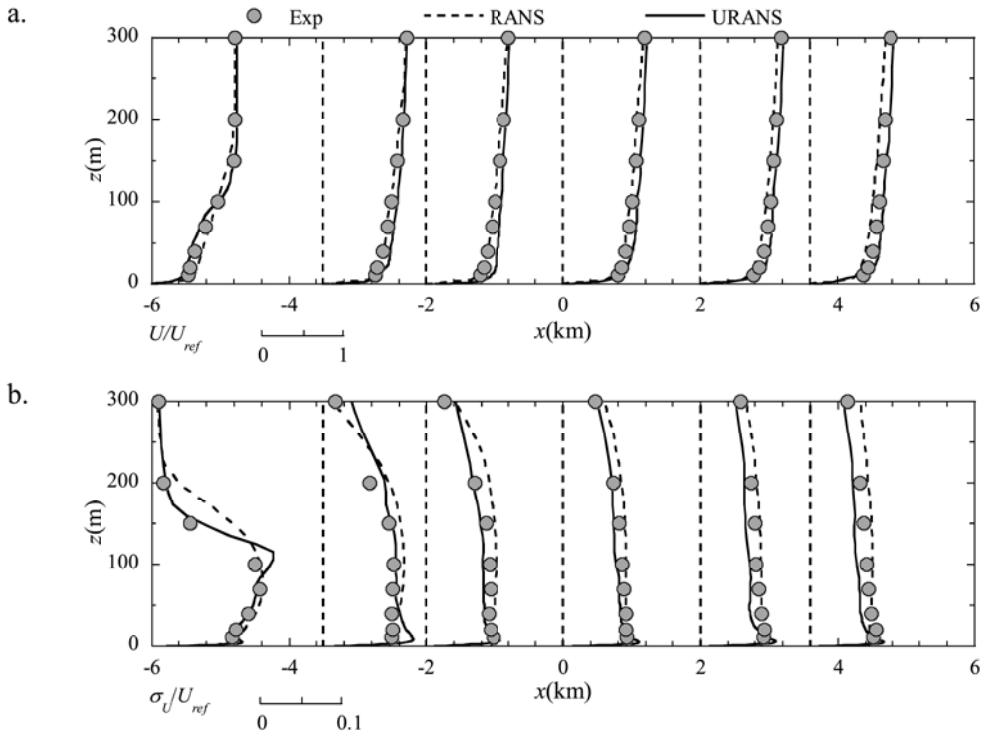

Fig. 7. Comparison of predicted and measured vertical profiles of (a) the mean and (b) standard deviation of streamwise velocities in the undisturbed boundary layer used for the case of complex terrain.

a grid stretching ratio of 1.15. The same grid system is used to perform numerical simulations for eight wind directions using. Similar to a turntable in a wind tunnel, the coordinates of the terrain are rotated when the wind direction changes. This terrain model is used to investigate the grid and time independence of turbulent flows over a complex terrain predicted by URANS.

3.3. Unsteady inflow and grid independence

The turbulent flow in the undisturbed boundary layer without complex terrain is first predicted using the computational domain as shown in Fig. 6 (a) and compared with the experimental data. In this section, an averaging time of 10 s is used in the URANS simulations. The

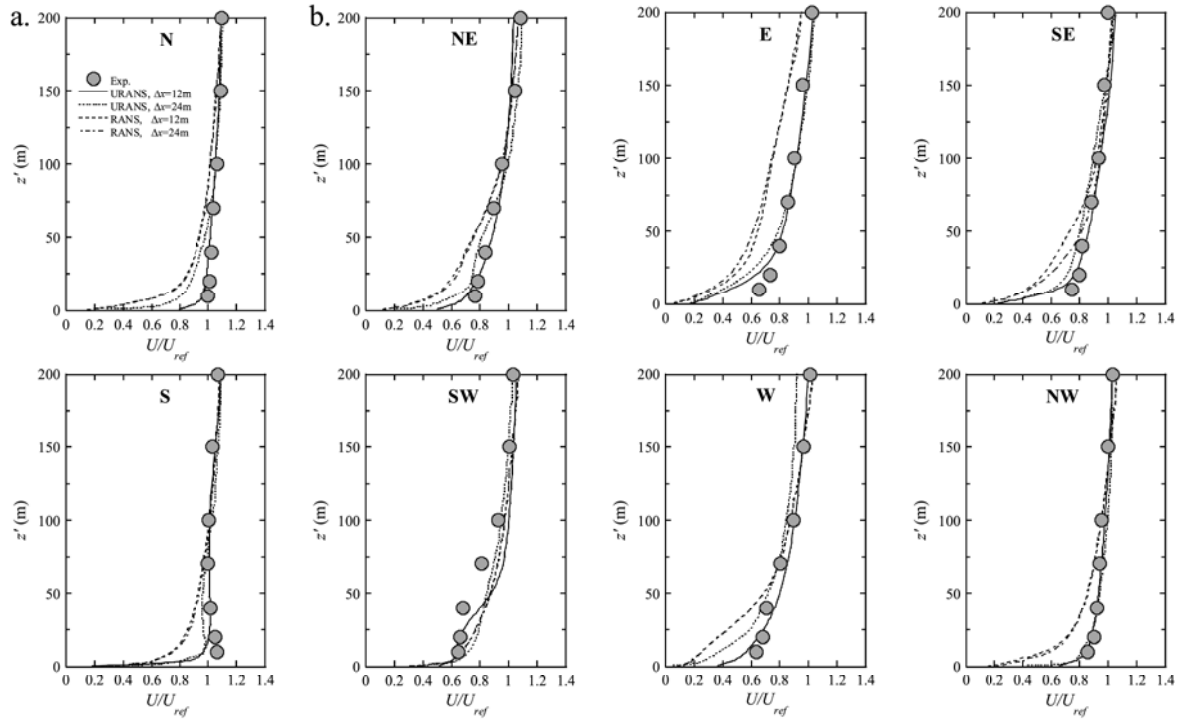

Fig. 8. Comparison of predicted and measured vertical profiles of (a)–(h) the mean streamwise velocity in eight wind directions at measurement point B shown in Fig. 3 (b).

standard deviation σ_u is calculated from turbulence kinetic energy K, i.e., $\sigma_u^2 = 1.2K$, as shown in Yamaguchi et al. (2003), which is based on the relation among the standard deviation of each velocity components obtained by Paterson and Holmes (1993). The predicted vertical profiles of the mean and standard deviation of the streamwise velocity in the undisturbed boundary layer are normalized by the wind speed outside the boundary layer U_{ref} as shown in Yamaguchi et al. (2003), and presented in Fig. 7. They are in good agreement with the experimental data, indicating that the generated unsteady inflow can be used to simulate the development of turbulent flow in an undisturbed boundary layer.

Ishihara et al. (2020) investigated the effect of grid resolutions on the simulation of flow fields in an urban area predicted by LES and RANS. The conclusion is that increasing the grid resolution significantly improves the prediction accuracy of LES, while the accuracy of RANS does not. This discrepancy in RANS is due to its inability to capture the coherent structure in the urban area by increasing the grid resolution.

The grid independence test is performed at measurement point B in complex terrain using two different grid resolutions of 12 m and 24 m in x and y directions, as shown in Fig. 3 (b). The averaging time of 10 s is also used in simulation for complex terrain. The vertical profiles of the mean and standard deviation of streamwise velocity at eight wind directions predicted by RANS and URANS models are illustrated in Figs. 8 and 9, respectively. The prediction accuracy of both the mean and standard deviation of streamwise velocity by RANS does not improve with increasing the grid resolution from 24 m to 12 m. For most wind directions, RANS underestimates the mean velocity and overestimates the standard deviation of velocity near the surface, which is consistent with the conclusions by Ishihara et al. (2020). This is because RANS cannot capture coherent structures near the surface (Uchida and Ohya, 2003; Ishihara and Qi, 2019; Ishihara et al., 2020). In contrast, the URANS with a grid resolution of 24 m shows slight inconsistencies with the experimental data, especially in the near-surface region, but performs well with a finer grid size of 12 m. A similar grid size of 12.5 m was used by Wang et al. (2024) and Cheng et al. (2024) to predict turbulent flows over real complex terrain. Compared with the grid size of LES and RANS as shown in Table 1, the optimal grid size of URANS is intermediate between LES and RANS, because URANS models small vortices, while resolving large eddies. This indicates that the computational efficiency of URANS is higher than that of LES. The grid size of 12 m in x and y directions is also used in Sections 4.1 and 4.2.

3.4. Optimal averaging times for different terrain slopes

The unsteady inflow used in this section is also examined. The computational domain is the same as that of Ishihara and Qi (2019). The predicted mean streamwise velocity and total turbulence kinetic energy in the undisturbed boundary layer at the location of the center of the hill are shown in Fig. 10, which are normalized by the wind speed U_{ref} as shown in Ishihara and Qi (2019). Both the mean streamwise velocity and turbulence kinetic energy also agree well with the experimental data. This indicates that URANS can accurately simulate both the resolved and modelled turbulence, resulting in the same total turbulent kinetic energy predicted by RANS.

To investigate the effect of terrain slope on the averaging time and recommend the optimal averaging time as a function of terrain slope, four hill heights are used as shown in Fig. 4. For each hill height, numerical simulations are conducted with three averaging times by URANS. The cases for determining the optimal averaging time as well as terrain slope index, criteria for terrain complexity and terrain complexity category as defined in IEC61400-1 (2019) are summarized in Table 3.

Simulations of the cases listed in Table 3 are conducted to determine the optimal averaging times for different terrain slopes. Fig. 11 displays the normalized mean velocity and total turbulence kinetic energy profiles over a three-dimensional hill with $H = 0.04$ m using URANS with different averaging times. With a proper averaging time, URANS accurately simulates the mean velocity and turbulence kinetic energy. As the averaging time increases, both the mean velocity and turbulence kinetic energy slightly decrease due to the reduced resolution of coherent structures in the wake region of the hill. Nevertheless, URANS is not sensitive to the averaging time compared to LES.

Numerical results for other terrain slopes are not presented in detail

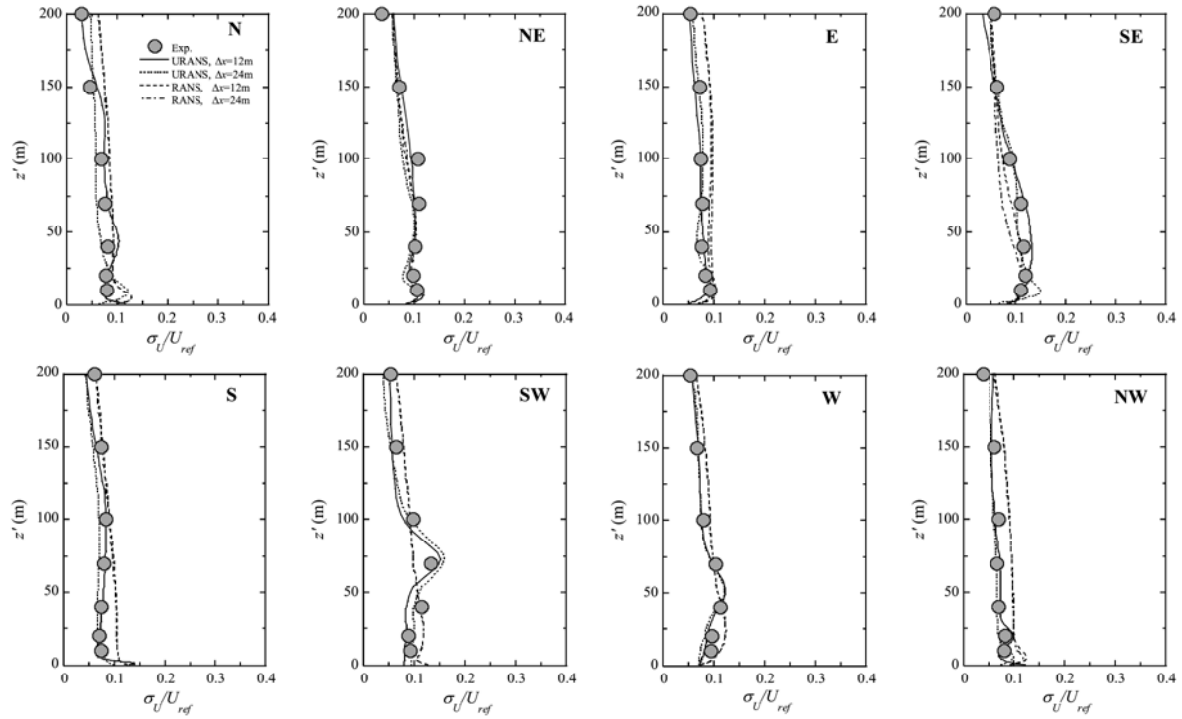

Fig. 9. Comparison of the predicted and measured vertical profiles of (a)–(h) the standard deviation of the streamwise velocity component in eight wind directions at measurement point B shown in Fig. 3 (b).

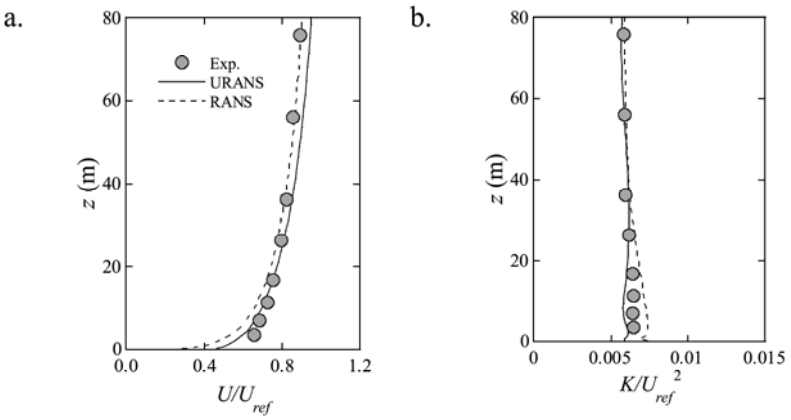

Fig. 10. Comparison of predicted and measured vertical profiles of (a) the mean streamwise velocity and (b) turbulence kinetic energy in the undisturbed boundary layer.

Table 3
Definition of criteria and category for terrain complexity in IEC61400-1 (2019)

Case	Hill height, H (m)	Terrain slope index, TSI (°)	Criteria for terrain complexity	Terrain complexity category	Averaging time, t_{ave} (s)
1	0.01	5.7	$0° < TSI < 10°$	Not complex	10, 20, 50
2	0.02	11.3	$10° < TSI < 15°$	*L*	
3	0.03	16.7	$15° < TSI < 20°$	*M*	
4	0.04	21.8	$TSI > 20°$	*H*	

here, but the performance of URANS for different terrain slopes is evaluated through the score as defined in Section 2.3. For H = 0.01, 0.02, 0.03 m, the numerical results from LES with $\Delta t = 0.0001$ s are used as the virtual observed values for the evaluation, since there are no experimental data for these three cases. Table 4 summarize the hit rates and scores of URANS for different terrain slopes and averaging times. The optimal averaging times for various terrain slopes are marked in red. As the terrain slope increases, the optimal averaging time decreases due to the more severe flow separation and the more high-frequency coherent structures, and therefore shorter averaging times are required to capture them accurately. The variation of the optimal averaging time with the terrain slope is shown in Fig. 12. The annotations 'Not complex', '*L*', '*M*', and '*H*' in Fig. 12 correspond to no, low, medium, and high terrain complexity in IEC61400-1 (2019), respectively. For the not complex terrain, the optimal averaging time is selected to be 50 s. For the terrain complexity index of *L*, 20 s can be selected. For terrain complexity indexes of *M* and *H*, 10 s is considered as the optimal averaging time. This averaging time, i.e., the time step used in URANS is one or two orders of magnitude larger than the time step used in LES as shown in Table 1. This indicates that the computational efficiency of URANS is much higher than LES.

The purpose of investigating the sensitivity of t_{ave} to terrain slope index of simple hill shapes is to determine the smallest t_{ave} that can be used to capture the vortex shedding. As can be seen from Table 4, for the terrain with a low TSI of 5.7 °, the optimal t_{ave} is larger than that with a high TSI of 11.3 ° or more, which is reasonable since vortex shedding of hill with low slopes is not as severe as these with high slopes. However, in engineering applications, complex terrain with both gentle and steep hills is very common, thus, the smallest t_{ave} = 10s should be adopted to capture vortex shedding and coherent structures in the wake region. Thus, the averaging time of 10 s is also used in numerical simulations over complex terrain in Sections 4.1 and 4.2. It is noticed that the proposed method is applied to several turbulent flow fields, such as a row of trees and a single building, and results with t_{ave} = 10s show good agreement with those by LES as shown in Qi and Ishihara (2018), which were validated by experimental data.

4. Turbulent flows over complex terrain in coastal regions

Section 4.1 presents the turbulent flow fields near measurement sites A and G, which are categorized as having gentle terrain. Section 4.2 shows the turbulent flow fields near measurement sites B and F, which are classified as having steep terrain.

4.1. Turbulent flow fields over gentle terrain around points A and G

Turbulent flow fields over gentle terrain at point A is first investigated. Fig. 13 illustrates the mean and standard deviation of streamwise velocities at point A in four typical directions predicted by RANS and URANS. The RANS model shows favorable good agreement with the experimental data for northerly and easterly winds in Fig. 13 (a) and (c) but underestimates the mean velocity near the ground for the southerly and westerly winds in Fig. 13 (b) and (d) due to the complex terrain upstream as shown in Fig. 2. In contrast, URANS provides favorable good agreement with the experimental data for all wind directions.

Fig. 14 visualizes the mean and standard deviation of streamwise velocities by URANS for a westerly in a horizontal plane of z' = 20m above the ground at measurement point A. Due to the effect of the terrain in the southwest, the mean velocity in the northeast is generally higher, while the standard deviation shows the opposite trend. In the wake region, the mean velocity is reduced, but the turbulent eddies cause larger standard deviations. This phenomenon is often seen in the

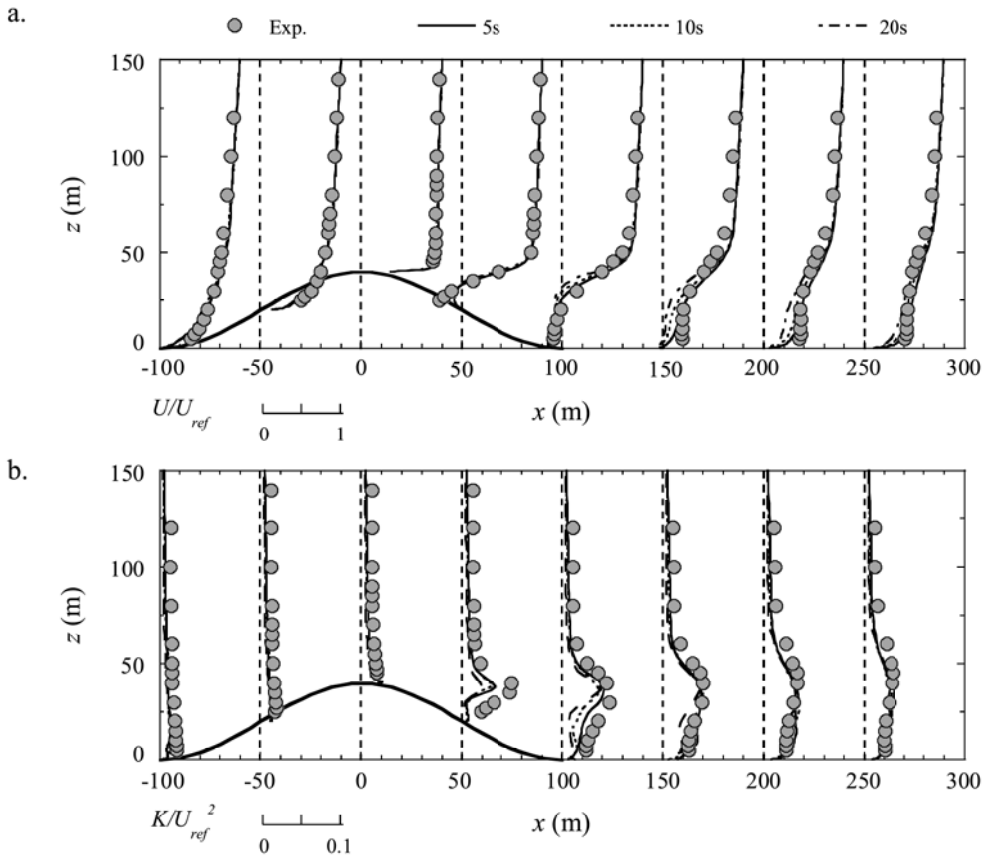

Fig. 11. Comparison of predicted and measured vertical profiles of (a) the mean streamwise velocity and (b) turbulence kinetic energy over a three-dimensional hill with $H = 0.04$ m on the vertical plane at $y = 0$.

Table 4
Variation of hit rate and score with terrain slopes and averaging times.

Terrain slope index, *TSI* (°)	t_{ave} (s)	q_U	q_K	S_a	T_{RANS} (h)	T (h)	S_e	S
5.7	10	1.00	0.90	1	0.35	2.64	3	3
	20	0.94	0.85	1		1.39	4	4
	50	0.89	0.83	1		0.67	5	5
11.3	10	0.92	0.90	1	0.35	2.66	3	3
	20	0.87	0.83	1		1.40	4	4
	50	0.82	0.75	0		0.69	5	0
16.7	10	0.89	0.90	1	0.36	2.67	3	3
	20	0.84	0.79	0		1.43	4	0
	50	0.77	0.64	0		0.68	5	0
21.8	10	0.86	0.89	1	0.38	2.70	3	3
	20	0.82	0.76	0		1.49	4	0
	50	0.76	0.43	0		0.72	5	0

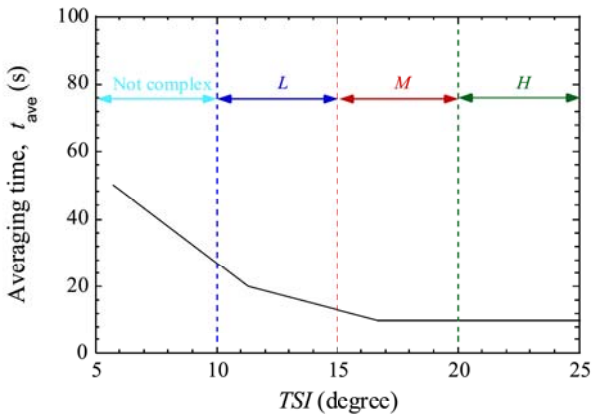

Fig. 12. Variation of optimal averaging time with terrain slope index.

wakes behind an obstacle due to the interaction between flow and terrain. URANS effectively captures low and high-speed streaks, as well as low and high turbulence streaks, while RANS cannot capture these streaks because it uses a uniform and steady inflow. This feature of URANS is similar to the LES used in Uchida and Ohya (2003). This explains why URANS achieves higher prediction accuracy compared to RANS at measurement point A.

Measurement point G is located on a relatively flat lowland with a small hill to the north and a ridge to the northeast. When the flow comes from the north or northeast, point G is in the wake region as shown in Fig. 2. Fig. 15 shows vertical profiles of the mean and standard deviation of streamwise velocities at point G in four typical wind directions predicted by RANS and URANS. RANS underestimates mean velocities of the northerly, northeasterly and southerly winds in Fig. 15 (a)–(c) compared to URANS due to the wake effect from upstream terrain but predicts the mean and standard deviation of the streamwise velocity of the southwesterly wind better in Fig. 15 (d) due to the flat upstream terrain. In contrast, URANS shows favorable good agreement with the experimental data for all wind directions.

To visualize the turbulent flow field in the wake region, Fig. 16 presents contours of the mean and standard deviation of streamwise velocities of the northeasterly wind by URANS. It is clear that URANS can reproduce the faster recovery of wake and accurately predict the standard deviation in the wake region. Since it is important to evaluate a strong mixing flow in the wake, it is recommended to use URANS for

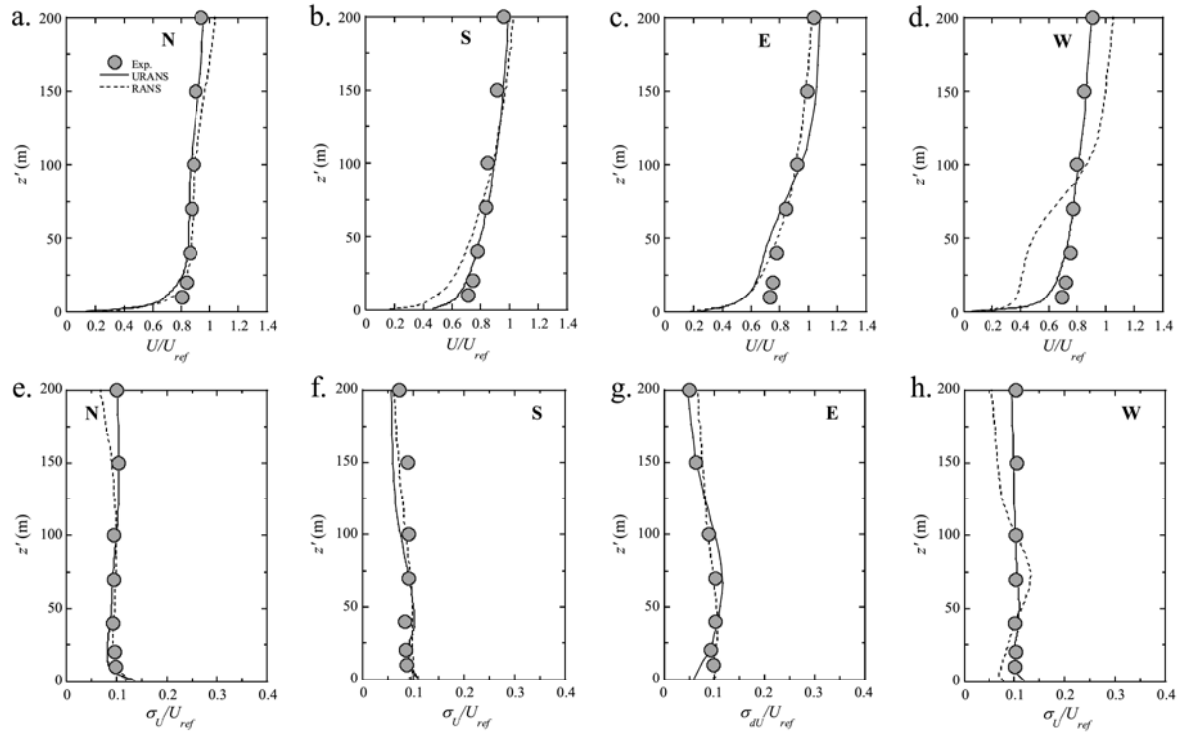

Fig. 13. Comparison of predicted and measured vertical profiles of (a)–(h) the mean and standard deviation of streamwise velocities at measurement site A in four typical wind directions.

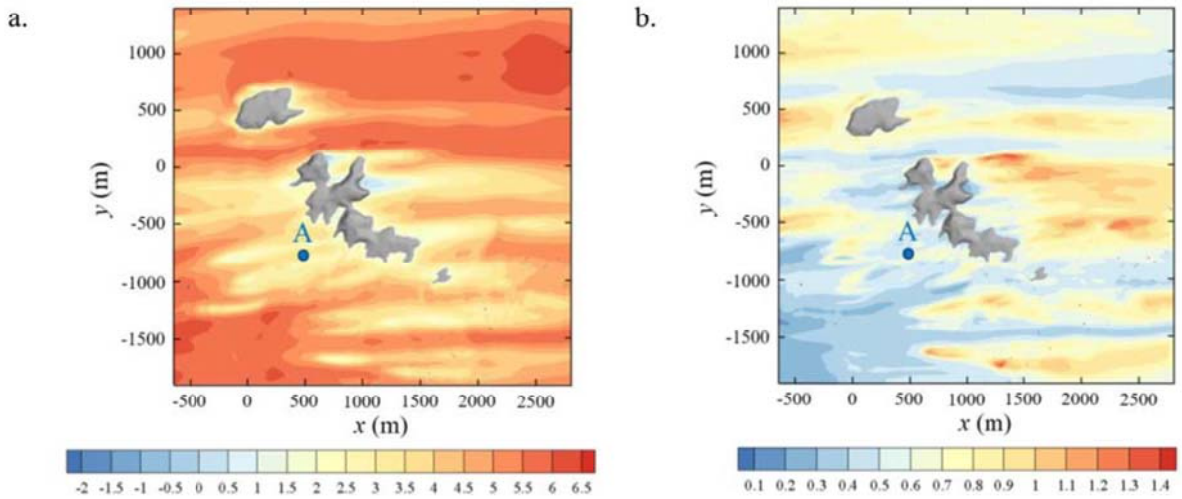

Fig. 14. Contours of (a) the mean and (b) standard deviation of streamwise velocities predicted by URANS for the westerly wind in the horizontal plane of $z' = 20$m above the ground at measurement point A. The units in the counter are m/s.

simulations even over relatively gentle terrain.

4.2. Turbulent flow fields over steep terrain around points B and F

Turbulent flow fields over steep terrain around point B are then investigated. As shown in Fig. 3 (b), the area around measurement point B features complex terrain. Fig. 17 illustrates the mean and standard deviation of streamwise velocities at site B for four typical wind directions predicted by RANS and URANS. RANS underestimates mean velocity of the northerly, northwesterly and westly winds near the ground in Fig. 17 (a)–(c) due to upstream complex terrain. In contrast, URANS accurately simulates both the mean velocity and standard deviation of streamwise velocities for all wind directions.

To evaluate the performance of URANS, Fig. 18 displays the mean and standard deviation of streamwise velocities at $z' = 20$ m and $z' = 70$ m above ground. At $z' = 20$ m, the mean velocity predicted by URANS responds quickly to the terrain and is consistent with the LES simulations over complex terrain by Abedi et al. (2021) as shown in Fig. 18 (a). In contrast, RANS assumes a time-averaged flow and neglects instantaneous fluctuations due to coherent structures, making it less sensitive to changes in terrain. Unsteady turbulence models such as URANS and LES consider time-dependent turbulence and better capture complex flow patterns. At $z' = 70$ m, the mean velocity predicted by RANS and URANS are similar, because the flow field at this height is less affected by the terrain.

As shown in Fig. 18 (b), the change in standard deviation of velocities

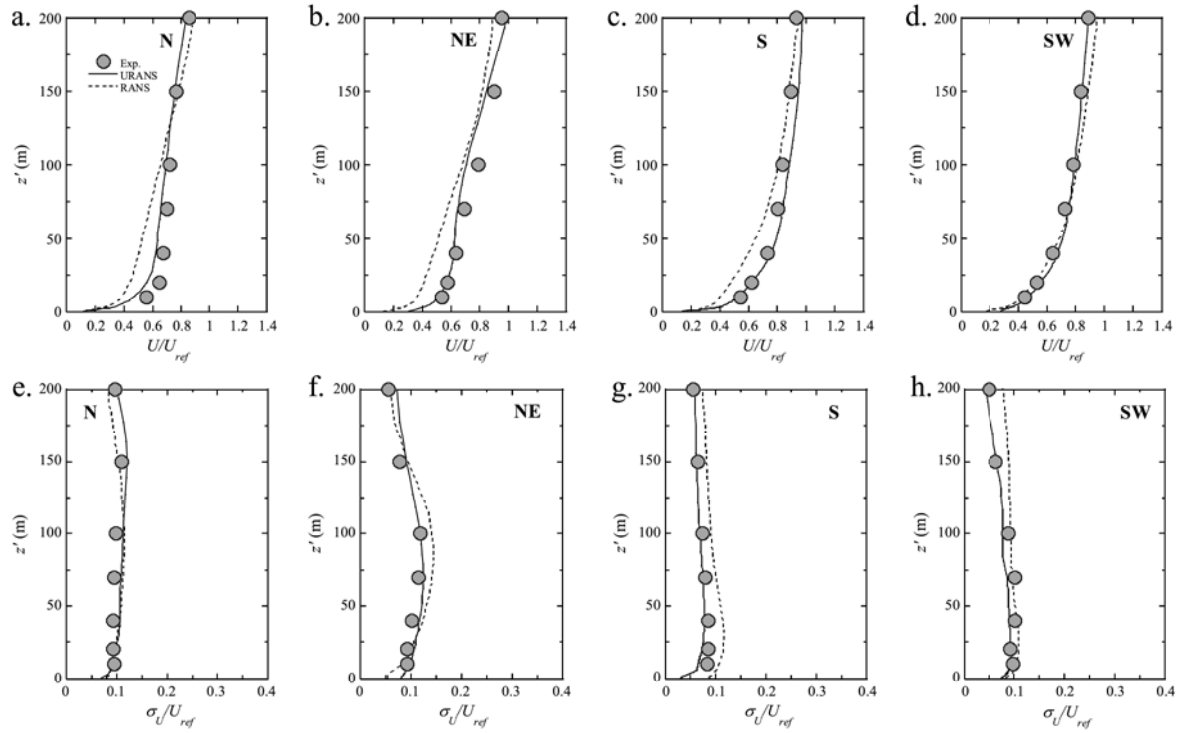

Fig. 15. Comparison of predicted and measured vertical profiles of the mean and standard deviation of the streamwise velocity at measurement site G in four typical wind directions.

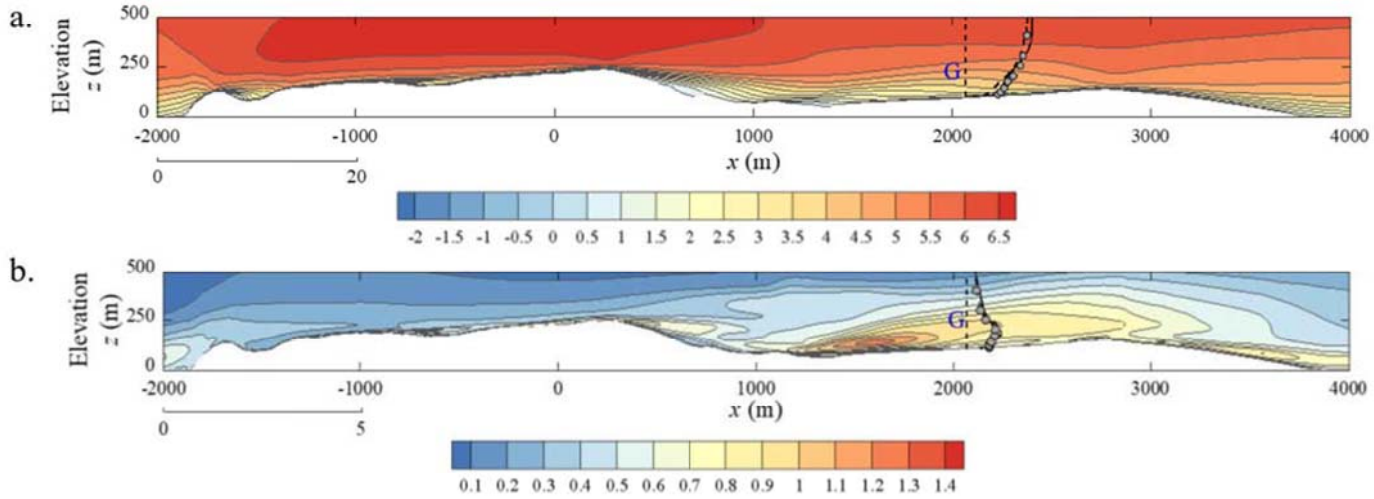

Fig. 16. Counters of (a) the mean and (b) standard deviation of streamwise velocities predicted by URANS for the northeasterly wind in the vertical plane across measurement point G. The vertical profiles of the mean and standard deviation of the streamwise velocity component at measurement point G are also shown in the counter. The units are m/s.

with terrain is less pronounced than that in mean velocity. At $z' = 20$m, the standard deviation of velocities predicted by URANS changes more pronounced with terrain compared to RANS for the same reason as the mean velocity. Furthermore, the standard deviation of velocity at $z' = 70$ m is higher than that at $z' = 20$ m due to the increased mean velocity and the increased turbulence.

Measurement point F is characterized by a steep cliff in Fig. 3 (c) and is used to compare RANS and URANS in reproducing flow separations. Fig. 19 illustrates the mean and standard deviation of streamwise velocities at point F for four typical wind directions predicted by RANS and URANS, RANS for the southeasterly and northwesterly winds in Fig. 19 (a) and (b) performs comparably to URANS as there is no flow separation. However, RANS for the northeasterly wind as shown in Fig. 19 (c) and (g) significantly overestimate the mean velocity and underestimate the standard deviation.

To explain why URANS can accurately predict the flow field of the northeasterly wind, Fig. 20 displays contours of the mean and standard deviation of streamwise velocities in the vertical plane across measurement point F. The contours show that the wind is blocked when it encounters a steep cliff, leading to flow separation and reattachment. The airflow reattaches downstream of the cliff, resulting in strong turbulent mixing. However, since RANS assumes that the airflow is time-averaged and steady, it cannot capture the unsteady motions in the recirculation zone, which reduces the prediction accuracy of the mean

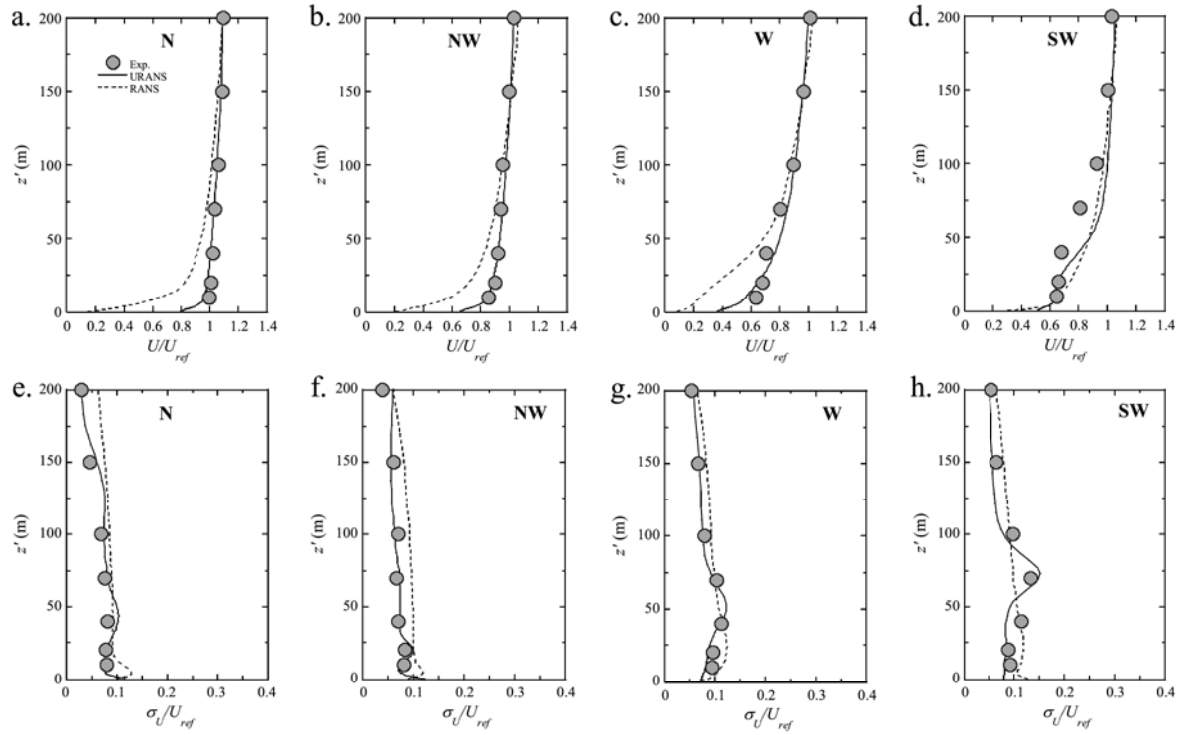

Fig. 17. Comparison of predicted and measured vertical profiles of the mean and standard deviation of streamwise velocities at measurement point B in four typical wind directions.

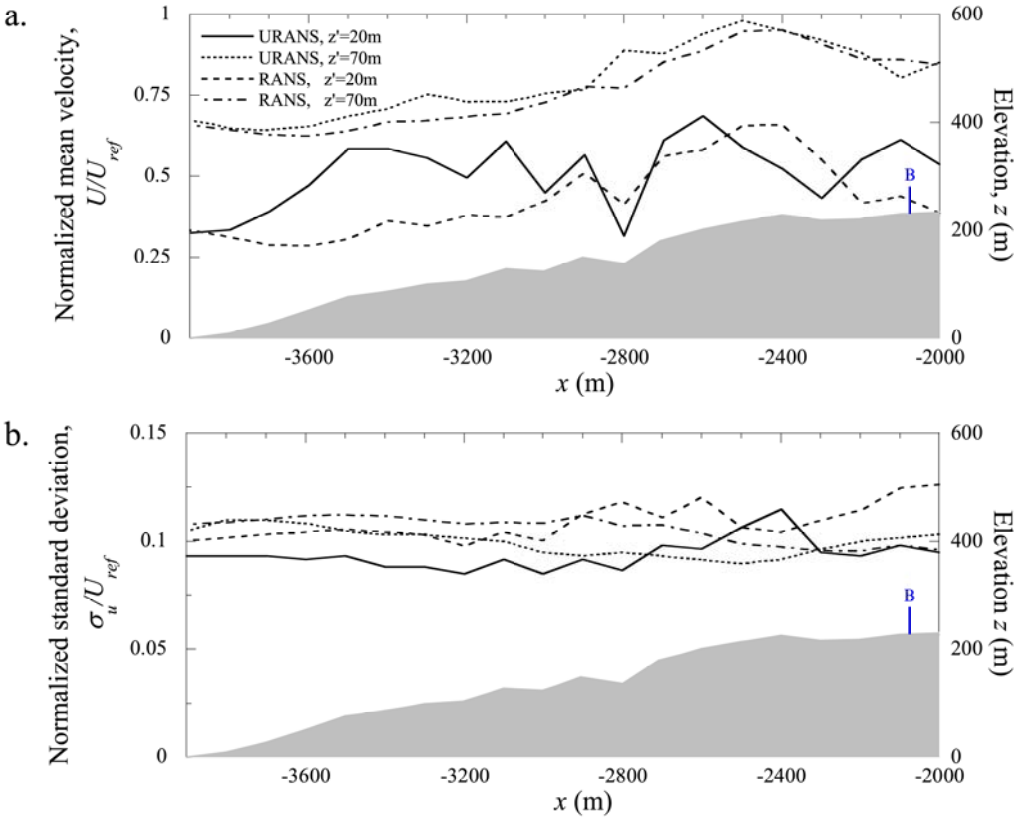

Fig. 18. The streamwise distributions of (a) mean and (b) standard deviation of streamwise velocities for the westerly wind at $z' = 20$ m and $z' = 70$ m above ground around measurement point B.

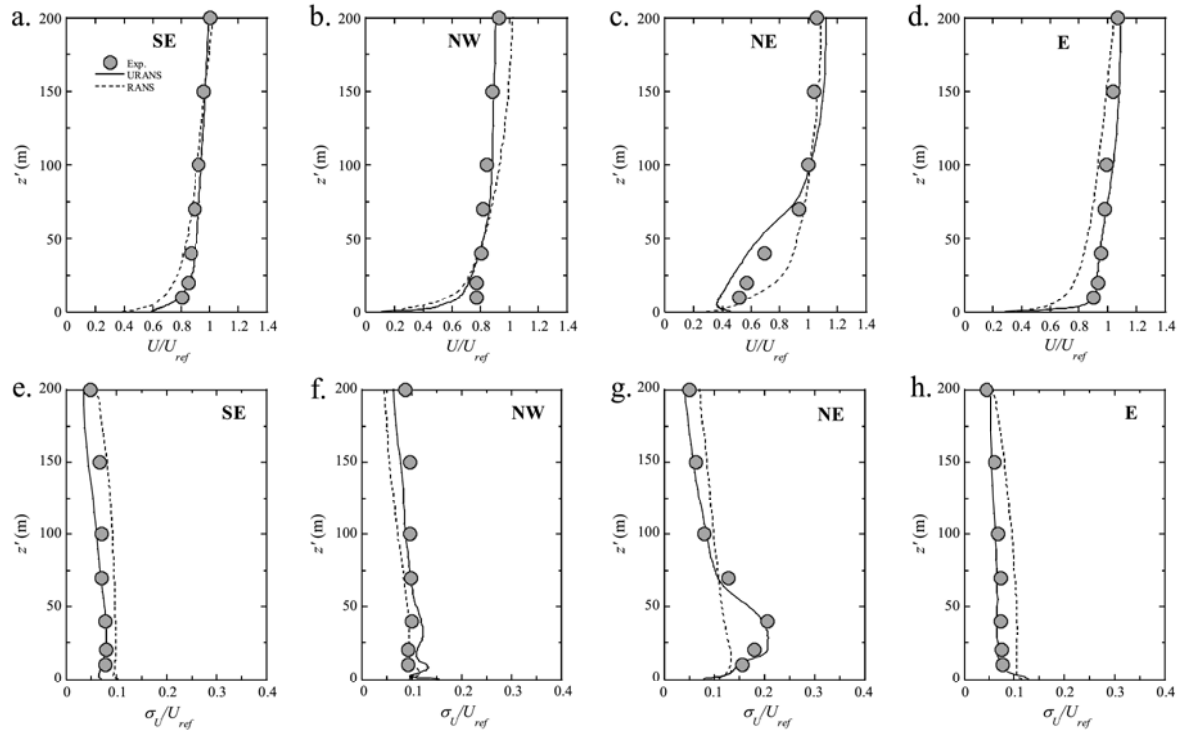

Fig. 19. Comparison of predicted and measured vertical profiles of the mean and standard deviation of streamwise velocities at measurement point F in four typical wind directions.

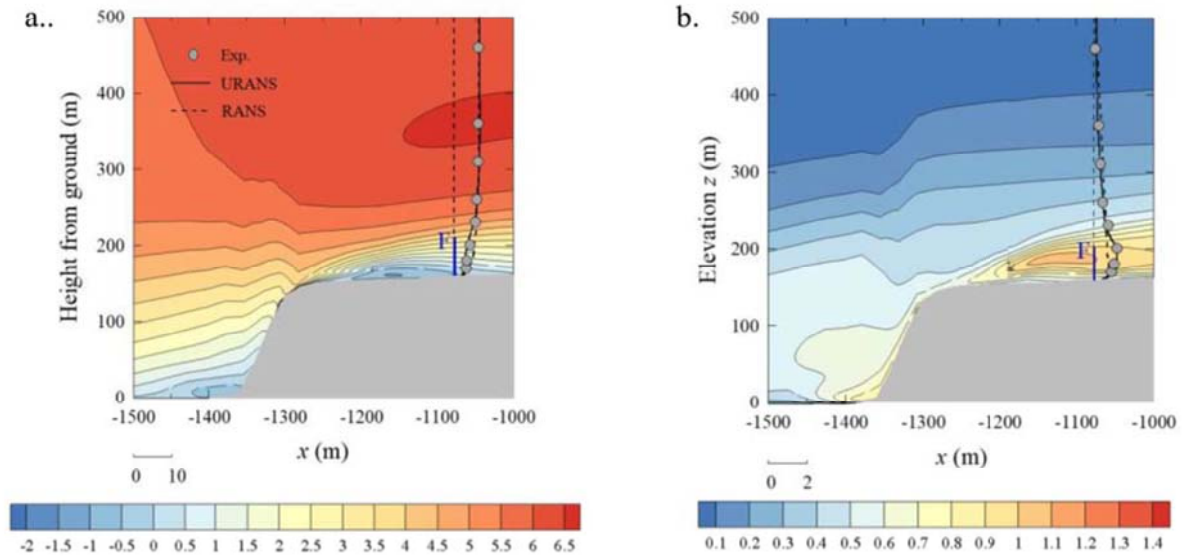

Fig. 20. Contours of (a) the mean and (b) standard deviation of streamwise velocities predicted by URANS for the northeasterly wind in the vertical plane across measurement point F. The vertical profiles of the mean and standard deviation of streamwise velocities at measurement point F are also shown in the counter. The units are m/s.

velocity and standard deviation. This limitation of RANS in predicting the flow fields around point F is similar to problem pointed out by Tominaga (2015) regarding the simulation of the reattachment zone above a single building, and highlights the superior performance of URANS in simulating turbulent flow over complex terrains.

5. Conclusions

In this study, an unsteady Reynolds-Averaged Navier-Stokes (URANS) model with a prespecified averaging time and a new method for turbulent inflow generation is proposed to predict turbulent flows over complex terrain. The following conclusions are obtained.

1. The effects of grid size on the mean velocity and standard deviation over complex terrain are investigated by URANS and RANS. URANS improves the accuracy of the predicted mean velocity and standard deviation by using a finer grid, but the RANS provides limited improvement because it models all the eddies in the turbulent flow fields over complex terrain. The optimal grid size of URANS for simulating turbulent flows over complex terrain is 12 m, which is intermediate between LES and RANS.
2. The turbulent flows over hills with four different slopes, corresponding to the terrain complexity index 'not complex', 'L', 'M' and 'H' in IEC61400-1, are investigated with URANS in terms of different averaging times. The optimal averaging time based on the slope of the hill is recommended considering the prediction accuracy and computational efficiency of URANS. When using URANS to simulate turbulent flows over complex terrain, an averaging time, i.e. a time step of 10 s is recommended. The time step is much longer than LES because URANS only resolves large eddies.
3. The turbulent wind fields over complex terrain in coastal regions are investigated with URANS. At measurement points A and G, the low and high-speed streaks and the mixing flows in the wake region are well captured by URANS. At measurement points B and F, the mean velocities predicted by URANS respond rapidly to the near-ground terrain and well show the separation, recirculation and reattachment of the flow behind the cliff, while RANS cannot capture these flow patterns well because a steady inflow is used in the simulations.

CRediT authorship contribution statement

Xiangyan Chen: Writing – original draft, Visualization, Software, Investigation, Formal analysis, Data curation. **Takeshi Ishihara:** Writing – review & editing, Validation, Supervision, Resources, Methodology, Conceptualization.

Declaration of competing interest

The authors declare that they have no known competing financial interests or personal relationships that could have appeared to influence the work reported in this paper.

Acknowledgements

This research is carried out as part of a joint program for next generation energy infrastructure with Toshiba Energy Systems & Solutions Corporation, J-POWER, Shimizu Corporation, Class NK, Tokyo Gas, CHOBU Electric Power. The authors express their deepest gratitude to the concerned parties for their assistance during this study. The authors also wish to thank the China Scholarship Council (Grant No. CSC202006130016) for the funding support.

Data availability

The authors do not have permission to share data.

References

Abedi, H., Sarkar, S., Johansson, H., 2021. Numerical modelling of neutral atmospheric boundary layer flow through heterogeneous forest canopies in complex terrain (a case study of a Swedish wind farm). Renew. Energy 180, 806–828. https://doi.org/10.1016/j.renene.2021.08.036.

Bao, X., Lou, W., Gu, Y., Liao, S., Lu, Z., Cai, W., 2024. Judgment criteria for significant wind speed-up regions in natural complex terrain. J. Wind Eng. Ind. Aerod. 249, 105724. https://doi.org/10.1016/j.jweia.2024.105724.

Beare, R.J., Macvean, M.K., Holtslag, A.A.M., Cuxart, J., Esau, I., Golaz, J.-C., Jimenez, M.A., Khairoutdinov, M., Kosovic, B., Lewellen, D., Lund, T.S., Lundquist, J.K., Mccabe, A., Moene, A.F., Noh, Y., Raasch, S., Sullivan, P., 2004. An intercomparison of large-eddy simulations of the stable boundary layer. Boundary-Layer Meteorol. 118, 247–272. https://doi.org/10.1007/s10546-004-2820-6.

Bechmann, A., Sorensen, N., 2011. Hybrid RANS/LES applied to complex terrain. Wind Energy 14 (2), 225–237. https://doi.org/10.1002/we.414.

Bhuiyan, M., Alam, J., 2020. Scale-adaptive turbulence modeling for LES over complex terrain. Eng. Comput. 38, 1995–2007. https://doi.org/10.1007/s00366-020-01190-w.

Blocken, B., 2014. 50 years of computational wind engineering: past, present and future. J. Wind Eng. Ind. Aerod. 129, 69–102. https://doi.org/10.1016/j.jweia.2014.03.008.

Blocken, B., Hout, A., Dekker, J., Weiler, O., 2015. CFD simulation of wind flow over natural complex terrain: Case study with validation by field measurements for Ria de Ferrol, Galicia, Spain. J. Wind Eng. Ind. Aerod. 147, 43–57. https://doi.org/10.1016/j.jweia.2015.09.007.

Chapman, D., 1979. Computational aerodynamics, development and outlook. AIAA J. 17 (12), 1293–1313. https://doi.org/10.2514/3.61311.

Chen, X., Liu, Z., Wang, X., et al., 2020. Experimental and numerical investigation of wind characteristics over mountainous valley bridge site considering improved boundary transition sections. Appl. Sci. 10 (3), 751. https://doi.org/10.3390/app10030751.

Cheng, X., Yan, B.W., Zhou, X.H., 2024. Wind resource assessment at mountainous wind farm: fusion of RANS and vertical multi-point on-site measured wind field data. Appl. Energy 363, 123116. https://doi.org/10.1016/j.apenergy.2024.123116.

Cheynet, E., Liu, S., Ong, M.C., Jakobsen, J.B., Gatin, I., 2020. The influence of terrain on the mean wind flow characteristics in a fjord. J. Wind Eng. Ind. Aerod. 205, 1–15. https://doi.org/10.1016/j.jweia.2020.104331.

Chipongo, K., Khiadani, M., Sookhak, L.K., 2020. Comparison and verification of turbulence Reynolds-averaged Navier–Stokes closures to model spatially varied flows. Sci. Rep. 10, 1–21. https://doi.org/10.1038/s41598-020-76128-9.

Feng, J., Xu, L., Baglietto, E., 2021. Assessing the applicability of the structure-based turbulence resolution approach to nuclear safety-related issues. Fluid 6 (61), 1–14. http://dx.doi.org/10.3390/fluids6020061.

Fluent, 2021. Ansys Fluent Theory Guide. Ansys Inc.

García, J., Munoz-Paniaguaa, J., Xu, L., Baglietto, E., 2020. A second-generation URANS model (STRUCT-ε) applied to simplified freight trains. J. Wind Eng. Ind. Aerod. 205, 1–11. https://doi.org/10.1016/j.jweia.2020.104327.

Hu, W., Yang, Q., Chen, H.P., et al., 2021. Wind field characteristics over hilly and complex terrain in turbulent boundary layers. Energy 224, 120070. https://doi.org/10.1016/j.energy.2021.120070.

Huang, W., Zhang, X., 2019. Wind field simulation over complex terrain under different inflow wind directions. Wind Struct. 28 (4), 239–253. https://doi.org/10.12989/was.2019.28.4.239.

IEC61400-1, 2019. Wind Energy Generation Systems-Part 1: Design Requirements, fourth ed. International Electrotechnical Commission.

Iizuka, S., Kondo, H., 2004. Performance of various sub-grid scale models in large-eddy simulations of turbulent flow over complex terrain. Atmos. Environ. 38, 7083–7091. https://doi.org/10.1016/j.atmosenv.2003.12.050.

Ishihara, T., Hibi, K., Oikawa, S., 1999. A wind tunnel study of turbulent flow over a three-dimensional steep hill. J. Wind Eng. Ind. Aerod. 83, 95–107. https://doi.org/10.1016/S0167-6105(99)00064-1.

Ishihara, T., Hibi, K., 2002. Numerical study of turbulent wake flow behind a three-dimensional steep hill. Wind Struct. 5 (2–4), 317–328. https://doi.org/10.12989/was.2002.5.2_4.317.

Ishihara, T., Qi, Y., 2019. Numerical study of turbulent flow fields over steep terrain by using modified delayed detached-eddy simulations. Boundary-Layer Meteorol. 170 (1), 45–68. https://doi.org/10.1007/s10546-018-0389-8.

Ishihara, T., Qian, G.W., Qi, Y., 2020. Numerical study of turbulent flow fields in urban areas using modified k-ε model and large eddy simulation. J. Wind Eng. Ind. Aerod. 206, 104333. https://doi.org/10.1016/j.jweia.2020.104333.

Israel, M.D., 2023. The myth of URANS. J. Turbul. 24 (8), 367–392. https://doi.org/10.1080/14685248.2023.2225140.

Lenci, G., 2016. A Methodology Based on Local Resolution of Turbulent Structures for Effective Modeling of Unsteady Flows. Dissertation, Massachusetts Institute of Technology, Cambridge, MA.

Li, J., Yang, X., Kunz, R.F., 2022. Grid-point and time-step requirements for large-eddy simulation and Reynolds-averaged Navier-Stokes of stratified wakes. Phys. Fluids 34, 1–9. https://doi.org/10.1063/5.0127487.

Li, Y., Yan, L., He, X., 2024. Large eddy simulation study of 3D wind field in a complex mountainous area under different boundary conditions. J. Zhejiang Univ. (Agric. Life Sci.) 25, 541–556. https://doi.org/10.1631/jzus.A2300613.

Liu, Z., Ishihara, T., He, X., Niu, H., 2016. LES study on the turbulent flow fields over complex terrain covered by vegetation canopy. J. Wind Eng. Ind. Aerod. 155, 60–73. https://doi.org/10.1016/j.jweia.2016.05.002.

Luis, T.W.C., 2012. Numerical Simulation of the Dynamics of Turbulent Swirling Flames. Technische Universität München, Munich, GER. Doctoral Dissertation.

Oettl, D., 2015. Quality assurance of the prognostic, microscale wind-field modelGRAL14.8 using wind-tunnel data provided by the German VDI guideline 3783-9. J. Wind Eng. Ind. Aerod. 142, 104–110. https://doi.org/10.1016/j.jweia.2015.03.014.

Paterson, D.A., Holmes, J.D., 1993. Computation of wind flow over topography. J. Wind Eng. Ind. Aerod. 46–47, 471–476. https://doi.org/10.1016/0167-6105(93)90314-E.

Qi, Y., Ishihara, T., 2018. Numerical study of turbulent flow fields around of a row of trees and an isolated building by using modified k-ε model and LES model. J. Wind Eng. Ind. Aerod. 177, 293–305. https://doi.org/10.1016/j.jweia.2018.04.007.

Qian, G.W., Ishihara, T., 2019. Numerical study of wind turbine wakes over escarpments by a modified delayed detached eddy simulation. J. Wind Eng. Ind. Aerod. 191, 41–53. https://doi.org/10.1016/j.jweia.2019.05.004.

Ren, H., Laima, S., Chen, W., Zhang, B., Guo, A., Li, H., 2018. Numerical simulation and prediction of spatial wind field under complex terrain. J. Wind Eng. Ind. Aerod. 180, 49–65. https://doi.org/10.1016/j.jweia.2018.07.012.

Schatzmann, M., Olesen, H., Franke, J., 2010. In: COST 732 Model Evaluation Case Studies: Approach and Results, p. 121. COST Office Brussels, ISBN, pp. 3–00.

Spalart, P.R., Jou, W.H., Strelets, M., Allmaras, S.R., 1997. Comments on the feasibility of LES for winds, and on a hybrid RANS/LES approach. In: Proceedings of the Advances in DNS/LES, pp. 1–11. Los Angeles.

Tominaga, Y., 2015. Flow around a high-rise building using steady and unsteady RANS CFD: effect of large-scale fluctuations on the velocity statistics. J. Wind Eng. Ind. Aerod. 142, 93–103. https://doi.org/10.1016/j.jweia.2015.03.013.

Uchida, T., Ohya, Y., 2003. Large-eddy simulation of turbulent airflow overcomplex terrain. J. Wind Eng. Ind. Aerod. 91, 219–229. https://doi.org/10.1016/S0167-6105(02)00347-1.

Vijiapurapu, S., Cui, J., 2010. Performance of turbulence models for flows through rough pipes. Appl. Math. Model. 34 (6), 1458–1466. https://doi.org/10.1016/j.apm.2009.08.029.

Wang, X., Hu, J., Deng, K., et al., 2024. Study on wind farm flow field characteristics based on boundary condition optimization of complex mountain numerical simulation. Processes 12 (9), 1885. https://doi.org/10.3390/pr12091885.

Watanabe, F., Uchida, T., 2015. Micro-siting of wind turbine in complex terrain: simplified fatigue life prediction of main bearing in direct drive wind turbines. Wind Eng. 39 (4), 349–368. https://doi.org/10.1260/0309-524X.39.4.349.

Xu, L., 2020. A Second Generation Unsteady Reynolds Averaged Navier Stokes Approach for Application to Aerodynamic Design and Optimization in the Automotive Industry. Dissertation, Massachusetts Institute of Technology, Cambridge, MA.

Yakhot, V., Orszag, S.A., 1986. Renormalization group analysis of turbulence. I. Basic theory. J. Sci. Comput. 1 (1), 3–51. https://doi.org/10.1007/BF01061452.

Yakhot, V., Smith, L.M., 1992. The Renormalization group, the e-expansion and derivation of turbulence models. J. Sci. Comput. 7 (1), 35–61. https://doi.org/10.1007/BF01060210.

Yamaguchi, A., Ishihara, T., Fujino, Y., 2003. Experimental study of the wind flow in a coastal region of Japan. J. Wind Eng. Ind. Aerod. 91, 247–264. https://doi.org/10.1016/S0167-6105(02)00349-5.

Yamaguchi, A., Tavana, A., Ishihara, T., 2024. Assessment of wind over complex terrain considering effects of topography, atmospheric stability and turbine wakes. Atmosphere 15 (6), 723. https://doi.org/10.3390/atmos15060723.

Yang, Q., Zhou, T., Yan, B., Liu, M., Pham, V.P., Shu, Z., 2021a. LES study of topographical effects of simplified 3D hills with different slopes on ABL flows considering terrain exposure conditions. J. Wind Eng. Ind. Aerod. 210, 104230. https://doi.org/10.1016/j.jweia.2020.104230.

Yang, Q., Zhou, T., Yan, B., Liu, M., Phuc, P., Shu, Z., 2021b. LES study of topographical effects of simplified 3D hills with different slopes on ABL flows considering terrain exposure conditions. J. Wind Eng. Ind. Aerod. 210, 104513. https://doi.org/10.1016/j.jweia.2020.104513.

Zhou, T., Yang, Q., Yan, B., Deng, X., Yuan, Y., 2022. Detached eddy simulation of turbulent flow fields over steep hilly terrain. J. Wind Eng. Ind. Aerod. 221, 104906. https://doi.org/10.1016/j.jweia.2022.104906.